

Bubble dynamics matters at high-rate water electrolysis

Received: 26 May 2025

Accepted: 25 January 2026

Published online: 03 February 2026

 Check for updates

Lizhen Wu¹, Qing Wang¹, Shu Yuan², Wenzhi Li¹, Xiaohong Zou¹, Mingcong Tang¹, Kouer Zhang¹, Xiaohui Yan²   & Liang An^{1,3}  

Bubbles accumulation in the electrode limits anion exchange membrane water electrolyzer performance at industrial current densities ($>1.0 \text{ A cm}^{-2}$). Currently, conventional electrode designs prioritize the optimization of the electrochemically active surface area. However, this study reveals that bubble dynamics matters high-rate water electrolysis efficiency in anode-feeding mode in three ways: 1) cover active sites at the anode; 2) hinder water diffusion through the membrane; 3) cause water shortage at the cathode. Based on this mechanism, we propose an easy-to-prepare gradient stainless steel square hole mesh electrode. It not only offers a low cost ($\$8\text{-}150/\text{m}^2$), but also improves bubble dynamics. As a result, it reduces the cell voltage by 0.14 V at a current density of 5.0 A cm^{-2} , even with a lower electrochemically active surface area compared to the stainless steel felt electrode. And it maintains a stable operation over 400 hours. This work redefines electrode engineering paradigms, shifting focus from electrochemically active surface area-centric approaches to two-phase flow management in water electrolyzers for industrial current densities-scale hydrogen production.

The transition to a net-zero carbon economy hinges on the swift implementation of scalable and cost-efficient green hydrogen production technologies^{1,2}. Water electrolysis, particularly when integrated with renewable energy, is the backbone of hydrogen production with minimal lifecycle carbon emissions^{3,4}. Within the spectrum of water electrolysis technologies, anion exchange membrane water electrolyzer (AEMWE) has garnered attention due to its advantageous combination of features derived from both alkaline water electrolyzer and proton exchange membrane water electrolyzer (PEMWE). These advantages include compatibility with non-precious metal catalysts, lower material costs, and the capability to operate at high current densities, etc^{5,6}. However, a major challenge lies in achieving industrial-scaled current densities while ensuring high efficiency and durability⁷. Addressing this challenge often requires enhancements in both oxygen evolution reaction (OER) activity and internal mass transport⁸⁻¹⁰.

As illustrated in Fig. 1, at lower current densities ($<1.0 \text{ A cm}^{-2}$)¹¹, the electrochemical performance of AEMWE primarily relies on the intrinsic activity and electrochemically active surface area (ECSA) of the catalyst. Many studies have concentrated on optimizing the morphology and composition of catalysts¹²⁻¹⁴, and electrode structures¹⁵⁻¹⁷ to enhance ECSA and charge transport kinetics. However, as current densities increase to fulfill industrial specifications ($>1.0 \text{ A cm}^{-2}$)¹¹, the effects of bubble dynamics on mass transport and interfacial processes become critically significant. The produced oxygen bubbles at the anode notably diminish the active sites of the electrodes¹⁸, disturb local pH and ion concentration gradients¹⁹, resulting in an elevated surface overpotential at a specific current density¹⁸. In addition, bubbles also hinder water diffusion through the membrane, and the diameter of the bubbles is related to the ohmic overpotential²⁰. Especially in the anode-feeding mode, bubble restrictions on water diffusion across the membrane lead to water shortage at the cathode, resulting

¹Department of Mechanical Engineering, The Hong Kong Polytechnic University, Kowloon, Hong Kong SAR, China. ²Institute of Fuel Cells, School of Mechanical Engineering, Shanghai Jiao Tong University, Shanghai, China. ³Research Centre for Carbon-Strategic Catalysis, The Hong Kong Polytechnic University, Kowloon, Hong Kong SAR, China. ✉e-mail: yanxiaohui@sjtu.edu.cn; liang.an@polyu.edu.hk

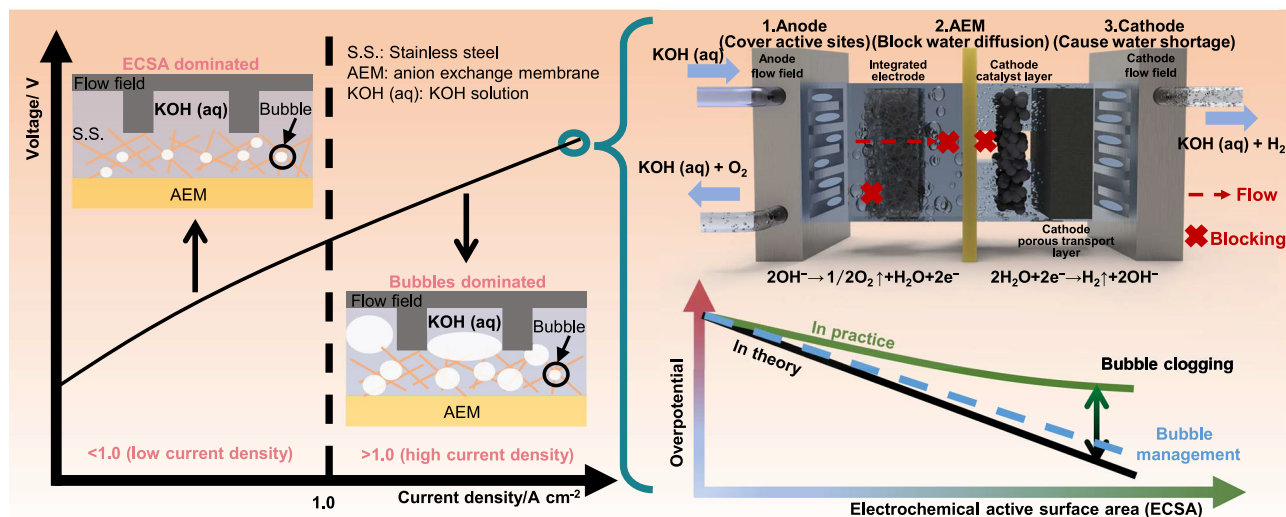


Fig. 1 | Bubble dynamics matters high-rate water electrolysis efficiency. The accumulation of anode bubbles impacts performance in three key ways: covering active sites at the anode, blocking water diffusion through the membrane, and

causing water shortage at the cathode. Therefore, increasing ECSA consistently will not ideally improve electrolyzer performance, proper bubble management is essential.

in insufficient supply of reactants²¹. Collectively, these factors diminish the efficiency and stability of the system. Consequently, effective bubble management at elevated current densities is important for improving the efficiency and stability of AEMWE.

Achieving effective bubble management can be accomplished at multiple scales. For example, some studies have focused on microstructural improvements^{22–24} or hydrophilic surface modifications^{25–27} at the microscopic level to achieve rapid bubble detaching from electrodes, and to mitigate mass transport overpotentials by renewing the electrolyte-electrode interface. Wan et al.²⁸ proposed a direct membrane deposition method for fabricating three-dimensionally (3D) ordered catalyst layers (CLs) on AEM, significantly improving AEM water electrolysis performance to rival that of state-of-the-art PEMWE by increasing the exposure of active sites, enhancing the gas/liquid mass transport, and hydroxide ion (OH^-) transport at the interface. The only drawback is the complexity of the processing methods and the need for careful handling. Ding et al.²⁹ presented an effective one-step method for creating an optimized OER substrate, demonstrating that a double-layered nickel (Ni) mesh with NiFe-layered double hydroxide can enhance mass transport and bubble management, leading to improved performance in AEMWE. In addition, at the macroscopic scale, Wu et al.³⁰ not only proposed a dual-layer channel flow field to improve the two-phase regimes in the flow channel and enabled the electrochemical performance of water electrolyzer to be enhanced by 0.15 V compared to that with the conventional serpentine flow field at a high current density of 5 A cm^{-2} , and also incorporates machine learning methods to optimize key parameters of this design³¹. It is believed that these recent studies on bubble dynamics in water electrolyzers will inform simpler and more efficient bubble management strategies.

Stainless steel felt has emerged as a highly attractive integrated anode electrode in AEMWEs, serving a dual function as both an efficient OER catalysts under alkaline conditions and the porous transport layer (PTL)^{32–34}. Its appeal lies in its relative ease of preparation and inherent structural robustness, offering a potentially cost-effective and durable alternative to more expensive catalyst-coated substrate electrodes³². Furthermore, in our previous research³⁵, we found that changes in the surface morphology of stainless steel felt, such as reduced surface hydrophilicity, lead to a decrease in the number of bubbles generated and an increase in the diameter of bubble detachment, obviously increasing activation and mass transport

overpotentials. Based on this, exploring multiple parameters such as pore size and hydrophilicity of stainless steel electrodes is a relatively simple and direct way to investigate which one of the electrode bubble dynamics and ECSA is the main factor affecting the electrochemical performance of AEMWE under high current conditions.

Herein, we employ a combination of techniques, including overpotential breakdown, distribution of relaxation times (DRT) analysis, potential measurements, and multiscale visualization methods, to explore the influence of bubble behaviors on mass transport and electrochemical performance in AEMWE with stainless steel electrodes that perform well under alkaline conditions. Firstly, it is demonstrated that enhancing bubble removal capabilities can substantially improve the electrochemical performance of electrodes with low ECSA. Therefore, we chose 316 L gradient stainless steel mesh. This design not only surpasses the electrochemical performance of stainless steel felt electrodes in AEMWE but also simplifies the conventional electrode preparation process while simultaneously enhancing energy efficiency and reducing anode fabrication costs by over 99.86% compared with traditional IrO_2 electrodes. This can also be seen as the systematic implementation of the “gradient structure + bubble control” strategy for AEMWE’s integrated stainless steel electrodes. The scientific positioning of this study is not on electrode design, but rather on using this design to reflect the more dominant role of bubble dynamics over electrode ECSA in AEMWE under high current conditions. Ultimately, this work highlights the need to balance ECSA optimization with two-phase flow management for high-rate operation. Addressing bubble-related mass transport issues could help improve the performance of future AEMWEs.

Results

Discovery of the dominant role of bubble dynamics at high current densities

Stainless steel electrodes have been shown to have strong OER activity under alkaline conditions, so we use an integrated (combined PTL and CL functions) stainless steel felt as the anode in this study^{32,35}. First, the anode-feeding configuration is selected based on its demonstrated advantages over cathode- or both-feeding modes (Supplementary Fig. 4), consistent with prior studies³⁶. Subsequently, the effect of the pore size of stainless steel felts on the electrochemical performance and bubble behaviors of AEMWE is investigated. Meanwhile, we

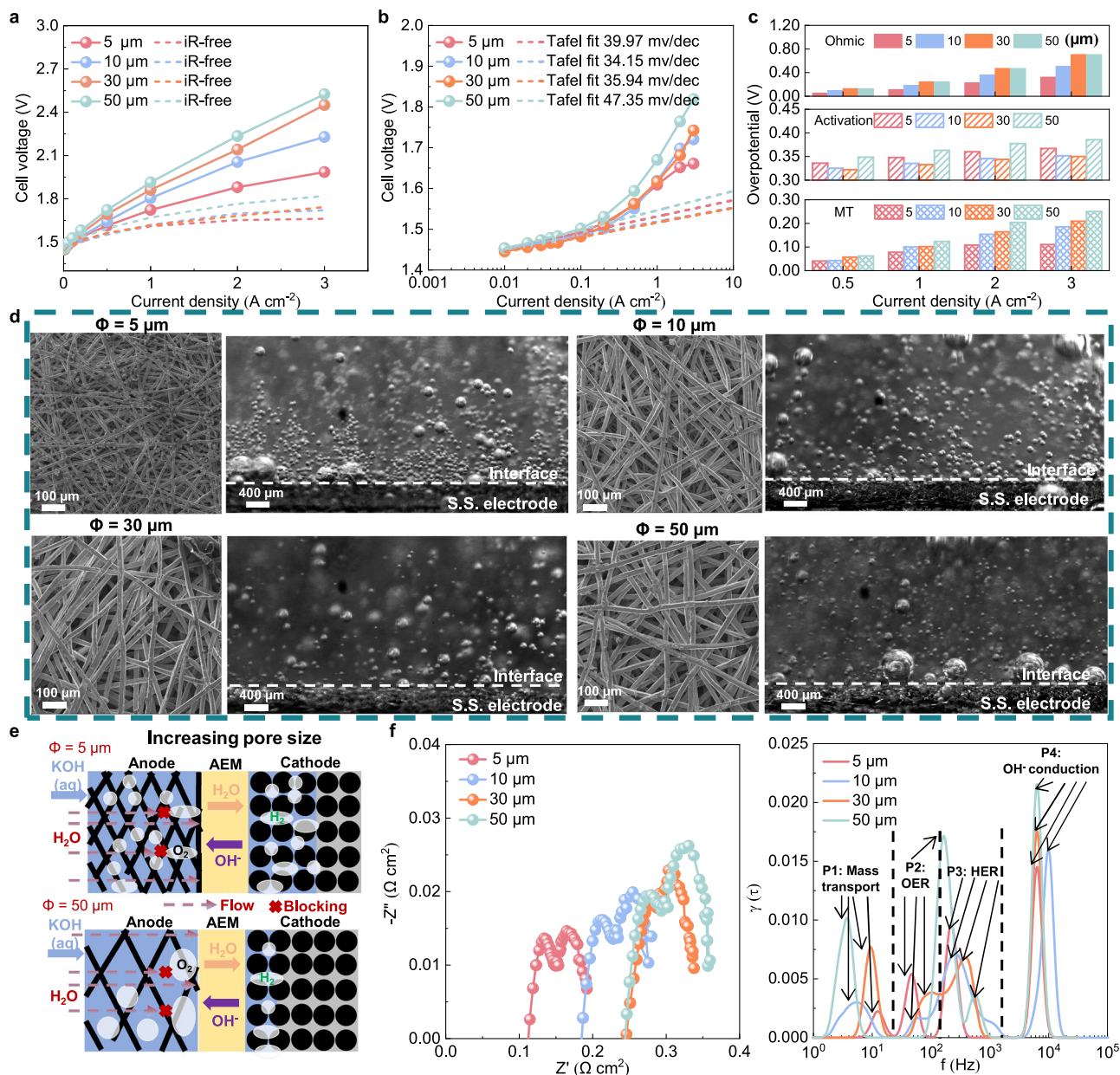


Fig. 2 | Pore size effects on performance and bubble dynamics. **a** Polarization and *iR*-free curves for AEMWE with the stainless steel felt-based anode with different pore sizes (geometric area: 4 cm², 2.0 × 2.0 cm). **b** Tafel slope and *iR*-free cell voltage. **c** Breakdown of each overpotential at different current densities. (operating conditions: 80 °C, PiperION A membrane (60 μm), the Pt/C cathode at a Pt loading of 0.5 mg cm⁻², the anode is supplied with 1 M KOH solution at 5 ml min⁻¹). MT: Mass transport. **d** SEM image and bubble behaviors in stainless steel felts with different pore sizes. Scale bar: 100 μm. (operating conditions: room temperature

(25 ± 2 °C), 0.4 A cm⁻², 1 M KOH, three electrode H-cell tests, in-plane direction parallel to the ground). **e** Schematic illustration depicting how varying pore sizes influence bubble behaviors at the anode and the diffusion of water through the membrane towards the cathode. **f** EIS curves and DRT analysis at 1.0 A cm⁻². ($\gamma(\tau)$: distribution of the relaxation times, (f) (Hz): characteristic frequency related to different electrochemical processes). Source data are provided as a Source Data file.

confirm the optimal torque and thickness of the stainless steel felt according to Supplementary Fig. 5 and Fig. 6, and in the following experiments, only the pore size of the stainless steel felt is varied (5–50 μm), which is determined in Supplementary Table 1 and Supplementary Fig. 7. As shown in Fig. 2a, reducing the pore size of the stainless steel felts significantly decreases the cell voltage at high current densities, with the 5 μm pore size electrode achieving better overall performance compared with other pore sizes. The internal resistance measured by high-frequency resistance (HFR) varies slightly at different current densities, as shown in Supplementary Fig. 10e. After excluding ohmic overpotential (*iR*-free (*E*–*iR*) curves), this trend persists. Through utilizing the Tafel approximation method³⁷, we

obtain Tafel slopes in Fig. 2b and breakdown of all overpotentials in Fig. 2c. Specifically, the ohmic overpotential takes up the majority of all overpotentials. A smaller pore size improves interfacial contact between the rib and the electrode³³, leading to reduced ohmic overpotential. For instance, a stainless steel felt with a 50 μm pore size results in over twice the ohmic overpotential compared to the 5 μm pore size felt. In addition, the activation and mass transport overpotentials in Fig. 2c are the sum of the cathode and anode, respectively, which was discussed in our previous study³⁵. The activation overpotentials have optimal values at 10 μm and 30 μm pore sizes felt. The 5 μm pore size felt shows the minimum mass transport overpotentials.

We try to draw some firm conclusions about the effect of electrode pore size on internal mass transport of AEMWE. However, it is difficult to determine directly which portion of the overpotential at the cathode and anode is affected by the pore size of the anode electrode only by the Tafel approximation method³⁵. Three-electrode configuration isolates the effect of anode pore size on OER performance (Supplementary Fig. 8a) and calculates the ECSA of all electrodes. For ECSA (Supplementary Fig. 8b), as the pore size increases, ECSA begins to decrease instead, which is consistent with performance differences at the low current density region in zero-gap membrane electrode assembly (MEA) electrolyzer (e.g., $<0.5 \text{ A cm}^{-2}$) (Supplementary Fig. 8c). A $5 \mu\text{m}$ pore size has the largest ECSA (Supplementary Fig. 8b and Fig. 9), it performs better than 30 and $50 \mu\text{m}$ but worse than $10 \mu\text{m}$. The only reason for this is that the $10 \mu\text{m}$ pore size is more conducive to bubbles removal than the $5 \mu\text{m}$ pore size, and the rapid bubble discharge reduces the coverage of the active sites and compensates for the relatively low ECSA of the electrode itself, as shown in Fig. 2d (also see Supplementary Movie 1). Incidentally, the oversized pore size facilitates bubbles removal but cannot compensate for the relatively low ECSA of the electrode itself, e.g., $50 \mu\text{m}$. Increasing pore size may not necessarily present smaller bubbles due to the thicker fibers and tortuous flow paths, increasing mass transport overpotentials³⁸. The view comes to the practical zero-gap MEA electrolyzer, which differs in that there is no physical isolation of the cathode and membrane from the anode in this system. Moreover, it is hypothesized that the bubbles and pore size at the anode also affect the water diffusing through the membrane to the cathode, leading to a complex situation different from the three-electrode tests, depicted in Fig. 2e. DRT method is able to directly extract the activation and mass transport impedance of the cathode and anode, respectively, in AEMWE. From Fig. 2f, smaller pores ($5 \mu\text{m}$) increase the OER-related impedance (P2 peak) due to untimely detachment of bubbles. Larger pores reduce hydrogen evolution reaction (HER) impedance (P3 peak) by enhancing water cross-membrane but exacerbate mass transport impedance (P1 peak) and OH^- transport (P4 peak) due to larger bubbles. The EIS curves at other current densities can be found in Supplementary Fig. 10, and stainless steel felt with different pore sizes also displays trend similar to those shown in Fig. 2f. Notably, the ohmic, activation, and mass transport impedances all decrease for each stainless steel felt as the current density increases. This occurs because higher current densities promote rapid bubble formation and release, which helps to efficiently eliminate bubbles from previous cycles and thereby reduce each impedance component. Finally, it can be expected that at low current densities, the electrochemical performance depends on the ECSA value. However, at high current densities, the bubble dynamics matters high-rate water electrolysis efficiency of AEMWE more than that of ECSA. The initial electrode design principle at high current densities can be summarized as ensuring sufficient ECSA and enabling rapid detachment while maintaining smaller bubble size, so that the activation and mass transport overpotentials can be both reduced.

Reconfirmation of key processes in AEMWE affected by bubble dynamics

We investigate the influence of surface wettability on AEMWE performance and its key processes through controlled modification of the fiber surface morphology of stainless steel felt while maintaining consistent pore structure. This can be regarded as a special experimental design, using diluted nitric acid (HNO_3) to reduce the ECSA of the stainless steel felts due to the oxidation of the fiber surface while enhancing its hydrophilicity by creating a roughened surface. This may better demonstrate whether bubble dynamics or ECSA plays the dominant role in AEMWE under high current densities conditions. Incidentally, compared to untreated samples, alcohol-washed stainless steel felts are cleaned with alcohol to remove grease and dirt. As

bubbles detach from the electrodes, grease and dirt on untreated samples are gradually washed away by the bubbles. As a result, their electrochemical performance and ECSA do not differ significantly (Supplementary Fig. 11), and alcohol-washed stainless steel felts are used as the base case in this section. In a three-electrode system, Fig. 3a, b demonstrate that the acid-washed stainless steel felt presents better performance than the alcohol-washed stainless steel felt (base case) in both OER performance and impedance, and the performance gap becomes more pronounced with increasing current density. Notably, while alcohol-washed stainless steel felt exhibits 2.3-fold higher ECSA ($3.81 \text{ mF cm}^{-2} > 1.65 \text{ mF cm}^{-2}$) than that of the acid-washed stainless steel felt (Fig. 3c and Supplementary Fig. 11), it fails to correlate with actual electrochemical performance. It suggests that evaluating electrode design solely based on ECSA may be insufficient under higher current densities.

Transitioning to a practical zero-gap MEA electrolyzer, acid-washed stainless steel felt achieves a 0.3 V voltage advantage over the alcohol-washed stainless steel felt at 5 A cm^{-2} (Fig. 3d). Using *iR*-free curves, the Tafel approximation method³⁷ is applied to determine the Tafel slope. The internal resistance measured by HFR varies slightly at different current densities, as shown in Supplementary Fig. 12c. In particular, compared with alcohol-washing, acid-washing increases the Tafel slope ($47.04 \text{ mV dec}^{-1}$ to $49.39 \text{ mV dec}^{-1}$) (Fig. 3e), which results in a significant increase in activation overpotentials at each current density. This reason may be that while the enhanced bubble dynamics of acid-washed felt improves bubble coverage on the electrode surface, it fails to sufficiently compensate for its inherently low ECSA. Nevertheless, this bubble dynamics enhancement yields more pronounced improvements in mass transport and ohmic overpotentials (Fig. 3f), ultimately resulting in a substantial overall performance enhancement through combined effects (Fig. 3d). The subsequent visualization results will help directly prove this hypothesis. The EIS and DRT analysis further resolves in detail that compared with the impedances of the alcohol-washed stainless steel felt, the anode activation impedance of the acid-washed stainless steel felt does not change significantly, the cathode activation impedance is lower, and the cathode and anode mass transport impedances are also both reduced (Fig. 3g), and this phenomenon becomes more obvious as the current density increases (Supplementary Fig. 12). The P4 peak shows the OH^- transport inside the electrode and at the interface, related to water movement. Acid-washed stainless steel felt has a smaller peak 4 area than alcohol-washed stainless steel felt, indicating lower OH^- transport impedance (Fig. 3g). This suggests that water transport from the anode to the cathode has been improved. Potential measurement in a customized electrolyzer (Supplementary Fig. 1) further validates this mechanism. Acid-washed stainless steel felt maintains a similar anode potential with alcohol-washed stainless steel felt, whereas alcohol-washed stainless steel felt exhibits significant cathode potential deviation at higher current densities (e.g., at 2.0 A cm^{-2}), directly mirroring the accuracy of the DRT analysis (Fig. 3h).

The exact reason for the performance improvement of AEMWE caused by acid-washed stainless steel felt can be attributed to the improved bubble dynamics, which optimizes its inside key processes: (1) Reduced active site coverage mitigates anode activation and mass transport polarization; (2) Promoted water across the membrane improves ohmic polarization; (3) Increased transmembrane water alleviates cathode water shortage-induced activation. Specifically, microscale visualization characterization is employed to elucidate the relationship between electrode structure, electrochemical performance, and bubble behaviors. Scanning electron microscopy (SEM) imaging (Fig. 4a, b) reveals acid-washing-induced surface roughening, while contact angle measurements confirm 38% hydrophilicity improvement (wetting time reduction from 56.6 to 41.1 ms), promoting faster bubble evolution³⁹. And in-situ bubble tracking³⁵ (Fig. 4a and d) quantifies optimized bubble management (also see Supplementary

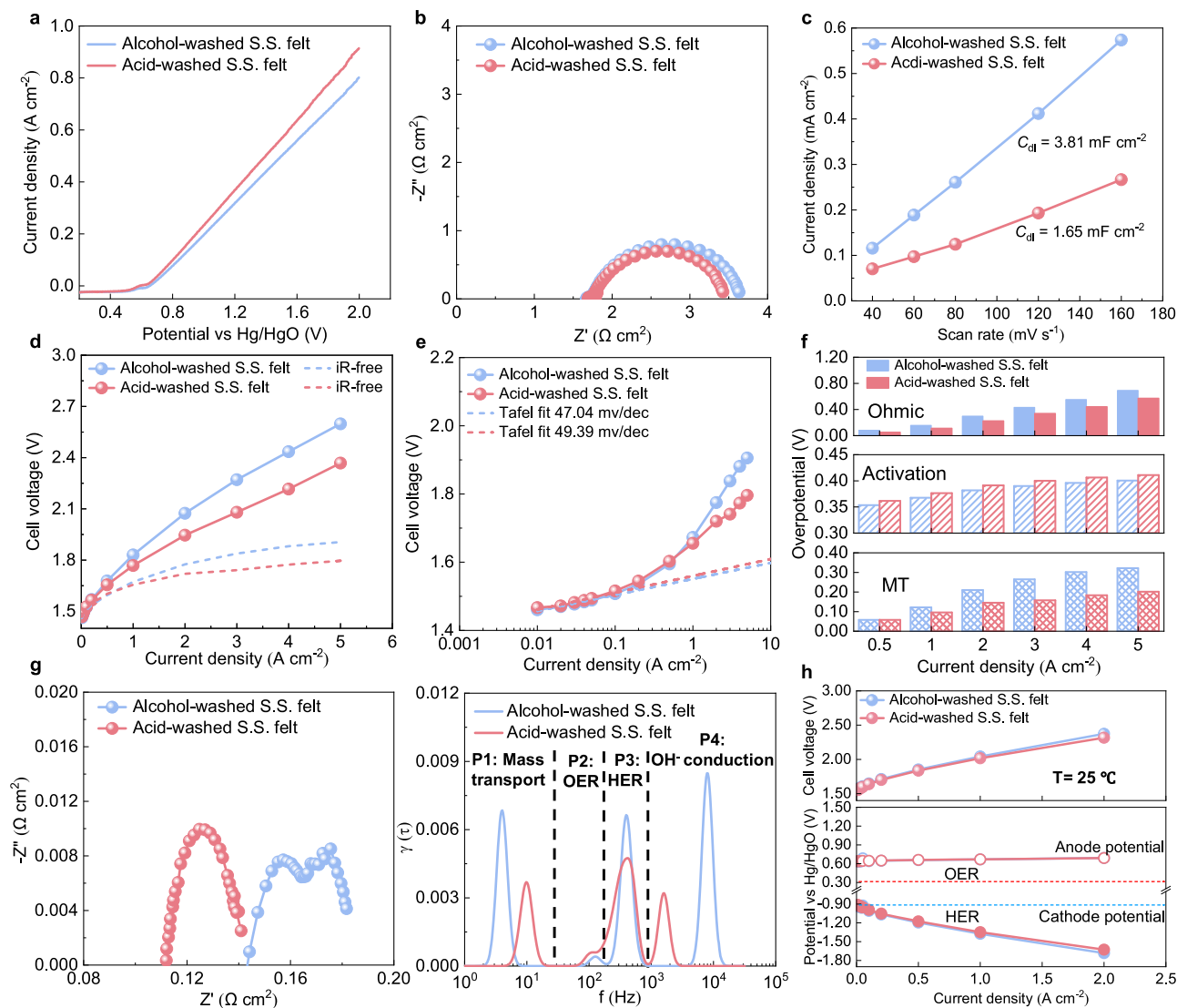


Fig. 3 | Hydrophilicity effects on electrochemical performance. Electrochemical performance of the alcohol-washed and acid-washed stainless steel (S.S.) felts in 1 M KOH through a standard three-electrode system (operating conditions: room temperature ($25 \pm 2^\circ\text{C}$), 1 M KOH): **a** LSV curves, **b** EIS curves. **c** Capacitive currents as a function of scan rate for ECSA (scan rate: 40–160 mV s^{-1}). C_{dl} : double-layer capacitance. Electrochemical performance of the alcohol-washed and acid-washed stainless steel felts through a zero-gap MEA system (geometric area: 4 cm^2 ,

$2.0 \times 2.0\text{ cm}$): **d** Polarization and iR-free curves. **e** Tafel slope and iR-free cell voltage. **f** Breakdown of each overpotential at different current densities. (operating conditions: 80°C , PiperION A membrane ($60\ \mu\text{m}$), the Pt/C cathode at a Pt loading of 0.5 mg cm^{-2} , the anode is supplied with 1 M KOH solution at 5 ml min^{-1}). MT: Mass transport. **g** EIS curves and DRT analysis at 3.0 A cm^{-2} . **h** Anode and cathode potentials of the AEMWE. Source data are provided as a Source Data file.

Movie 2). Acid-washed stainless steel felt generates 20% smaller bubbles (56.4 to $44.9\ \mu\text{m}$ diameter) with 33% higher number density (126 to 168 counts). This can reduce coverage and mass transport resistance on the electrode surface⁴⁰. Crucially, the acid-washed stainless steel felt also consistently presents better OER performance under the constant-current test (Fig. 4c), proving the above key process (1). Direct monitoring of cathode-collected water (Fig. 4f) substantiates the above key processes (2) and (3). Finally, this improved bubble dynamics is ultimately identified as improving performance through the above three key processes (Fig. 4e). In addition, the duration of the performance gap between the acid-washed stainless steel felt and the alcohol-washed stainless steel felt is noteworthy. Initially, the acid-washed stainless steel felt presents better performance than the alcohol-washed stainless steel felt. However, their voltages become similar after approximately 30 h, and by around 85 h, the acid-washed stainless steel felt surpasses the alcohol-washed stainless steel felt (Supplementary Fig. 13a). After 120 h, both electrodes show significant degradation in electrochemical performance (Supplementary Fig. 13b)

and ECSA (Supplementary Figs. 13c and 14), with the alcohol-washed stainless steel felt maintaining a higher ECSA throughout (Supplementary Fig. 13c). EIS data indicate that increased OER impedance is the main reason for the performance decline in the long term (Supplementary Fig. 13d). Specifically, SEM images (Supplementary Fig. 15) reveal that the fresh acid-washed stainless steel felt has a slightly rougher surface than the alcohol-washed stainless steel felt. XPS analysis (Supplementary Fig. 16) shows that diluted HNO_3 etching forms a dense chromium-rich oxide layer. Although this layer reduces ECSA, it improves initial hydrophilicity (Supplementary Fig. 17) and bubble dynamics (Supplementary Fig. 18), explaining the early-stage performance advantage. Over time, the surface morphology of the two electrodes becomes similar (Supplementary Fig. 15). After 120 h, the decrease in oxyhydroxides and the significant loss of Cr, Fe, and Ni lead to reduced hydrophilicity and fewer active sites (Supplementary Fig. 16). As a result, the decreased ECSA and worsened bubble removal (Supplementary Fig. 19) become the primary reasons for the increased OER impedance and performance degradation of the acid-washed

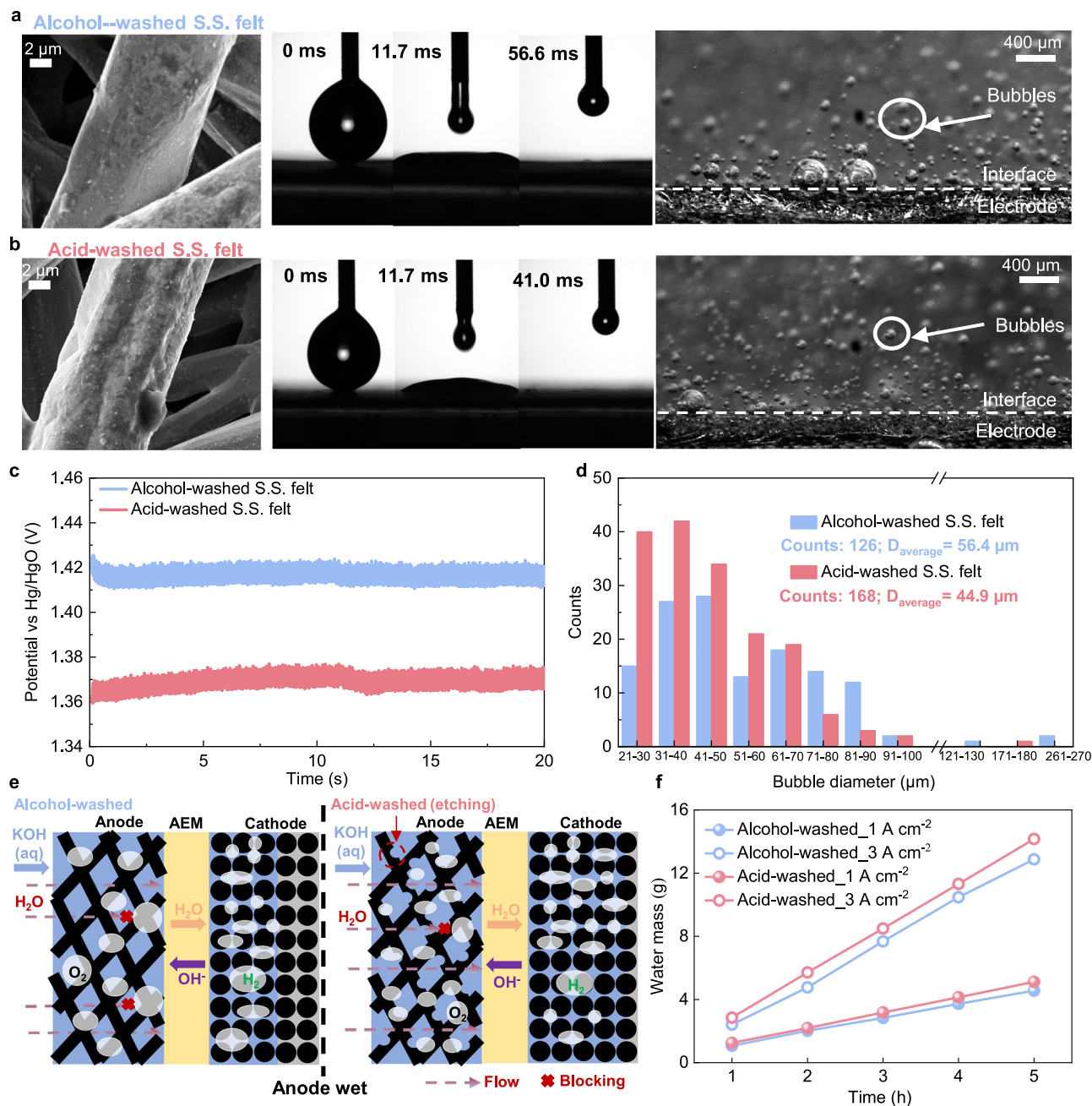


Fig. 4 | Hydrophilicity effects on bubble behaviors and water transport. SEM image, contact angle tests, and bubble behaviors in stainless steel (S.S.) felts. (operating conditions: room temperature ($25 \pm 2 \text{ }^\circ\text{C}$), 0.4 A cm^{-2} , 1 M KOH , three electrode H-cell tests, in-plane direction parallel to the ground): **a** Alcohol-washed stainless steel felt. **b** acid-washed stainless steel felt. Scale bar of electrode morphology: $2 \mu\text{m}$, Scale bar of bubble visualization: $400 \mu\text{m}$. **c** Time transition of

potential vs Hg/HgO at 0.4 A cm^{-2} . **d** The distribution of bubble sizes counted in high-speed camera images. **e** Schematic illustration depicting how hydrophilicity influences bubble behaviors at the anode and the diffusion of water through the membrane towards the cathode. **f** The amount of water collected at the cathode across the membrane as a function of time for AMEWEs with alcohol-washed and acid-washed stainless steel felts. Source data are provided as a Source Data file.

stainless steel felt after prolonged operation. Therefore, it is not recommended to use diluted HNO_3 to treat stainless steel felt in industrial water electrolysis applications. This can be viewed as a special experimental design (reduced ECSA but improved bubble dynamics) to validate whether ECSA or bubble dynamics is the key factor to dominate the performance of AEMWE at high current densities. In addition, we also add hydrochloric acid (HCl) treatment samples to mitigate the surface oxidation, which not only increases ECSA but also presents better performance than alcohol-washed stainless steel felt (Supplementary Figs. 20–22).

In contrast, it is also worth mentioning that increasing ECSA to the same electrode substrate but deteriorating its bubble

dynamics may degrade performance at high current densities, as its effect depends on the chosen method. For example, the morphology and surface composition of IrO_2 + ionomer-coated stainless steel felt are shown in Supplementary Figs. 23–25. When using piperION ionomer, an about 60% increase in ECSA, as the current density increases to 5.0 A cm^{-2} , the iR-free cell voltage gap with uncoated stainless steel felt gradually narrows to a negligible level. When using Nafion ionomer, the AEMWE performance worsens by about 600 mV at 5.0 A cm^{-2} , despite an about 123% increase in ECSA (Supplementary Figs. 26 and 27). The bubble behaviors detach from the above three electrodes help explain these differences (Supplementary Fig. 28).

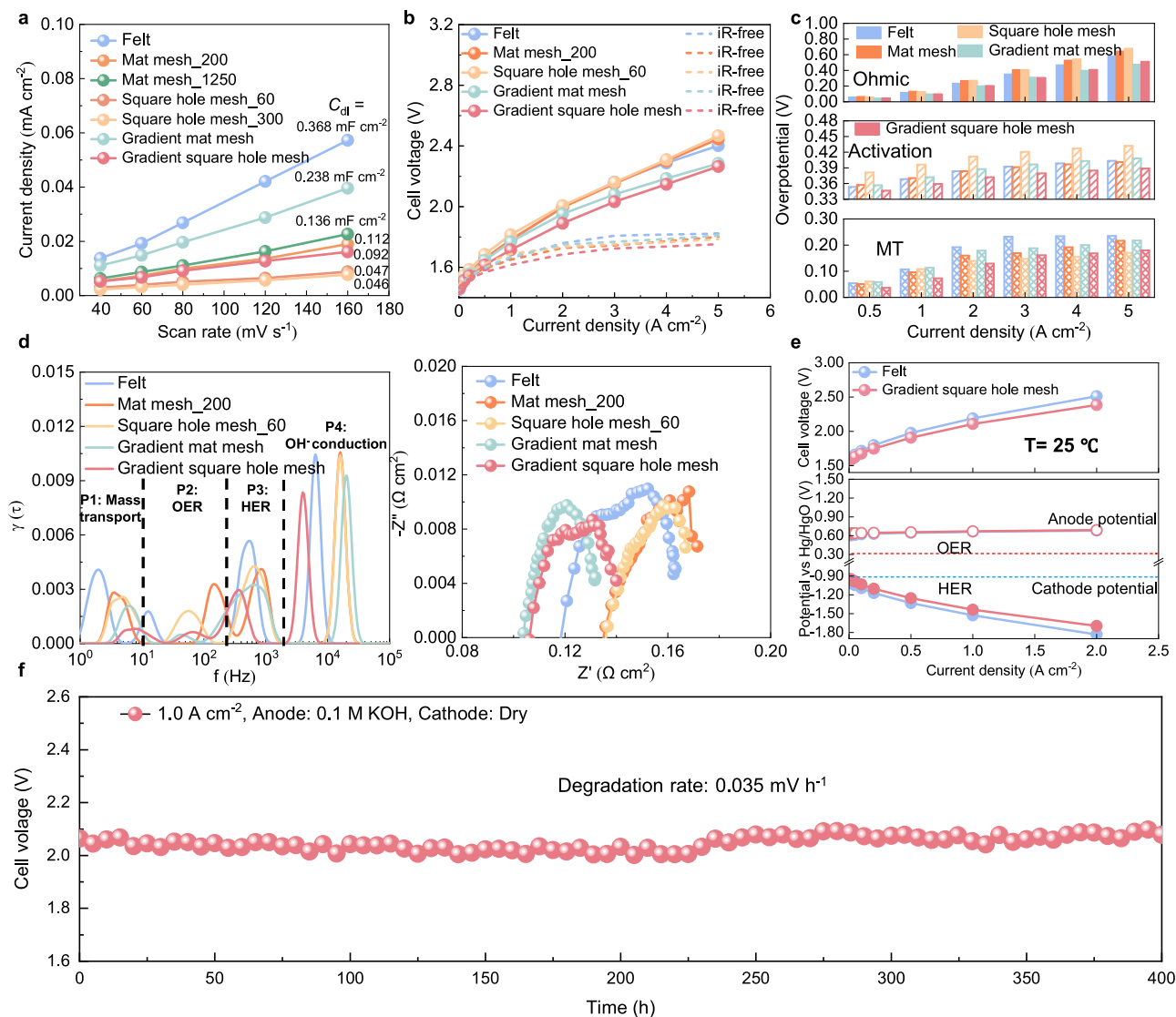


Fig. 5 | The gradient square hole mesh design enhances performance and durability. **a** Capacitive currents as a function of scan rate for ECSA (scan rate: 40–160 mV s⁻¹). (operating conditions: room temperature (25 ± 2 °C), 1 M KOH). C_{dl} : double-layer capacitance. Electrochemical performance of the different stainless steel mesh designs through a zero-gap MEA system (geometric area: 4 cm², 2.0 × 2.0 cm): **b** Polarization and iR-free curves. **c** Breakdown of each overpotential

at different current densities. (operating conditions: 80 °C, PiperION A membrane (60 μm), the Pt/C cathode at a Pt loading of 0.5 mg cm⁻², the anode is supplied with 1 M KOH solution at 5 ml min⁻¹). MT: Mass transport. **d** EIS curves and DRT analysis at 3.0 A cm⁻². **e** Anode and cathode potentials of the AEMWE. **f** AEMWE durability using gradient stainless steel square hole mesh at a current density of 1.0 A cm⁻². Source data are provided as a Source Data file.

Advantages of the gradient stainless steel mesh and operational stability

To enhance bubble removal and water transport at high current densities, we have designed a stainless steel mesh electrode with a gradient structure. Firstly, three-electrode configuration reveals that the non-gradient square hole mesh with sieves of 300 exhibits the worst OER performance, whereas gradient designs (both mat and square hole) demonstrated better performance at high current densities and even the gradient square hole mesh is better than all other designs (Supplementary Fig. 29). Critically, ECSA measurements (Fig. 5a and Supplementary Fig. 30) depict that the gradient square hole mesh is even lower than the non-gradient mat mesh with sieves of 200 or 1250, and is a quarter of the ECSA of the felt. Transitioning to a practical zero-gap MEA electrolyzer test, gradient stainless steel square hole mesh presents better performance compared to all other stainless steel electrode designs, achieving a cell voltage reduction of 0.14 V at 5 A cm⁻² compared with stainless steel felt (Fig. 5b). In addition, mat mesh with sieves of 200 and square hole mesh with sieves of 60 exhibit

cell voltages very close to those felt. Specifically, through the Tafel approximation (Supplementary Fig. 31), we obtain the breakdown for each overpotential (Fig. 5c). The internal resistance measured by HFR varies slightly at different current densities, as shown in Supplementary Fig. 33f. In terms of ohmic overpotentials, mat mesh and square hole mesh have higher ohmic overpotentials due to their more pronounced localized surface heights, which do not ensure good interfacial contact with the rib of the flow field plate (Fig. 6a and Supplementary Fig. 32). By contrast, the gradient mat mesh and gradient square hole mesh may improve the bubbles removal from the anode to a large extent and significantly increase the water content of the membrane and cathode. Even with poor interfacial contact, they can also lower the ohmic overpotential. In terms of activation and mass transport overpotentials, the gradient square hole mesh is much lower than the other designs. DRT and EIS analyses (Fig. 5d and Supplementary Fig. 33) indicate that the anode impedance of gradient square hole mesh is close to that of the felt, but the cathode impedance is much lower than that of the felt. For the gradient mat mesh, its

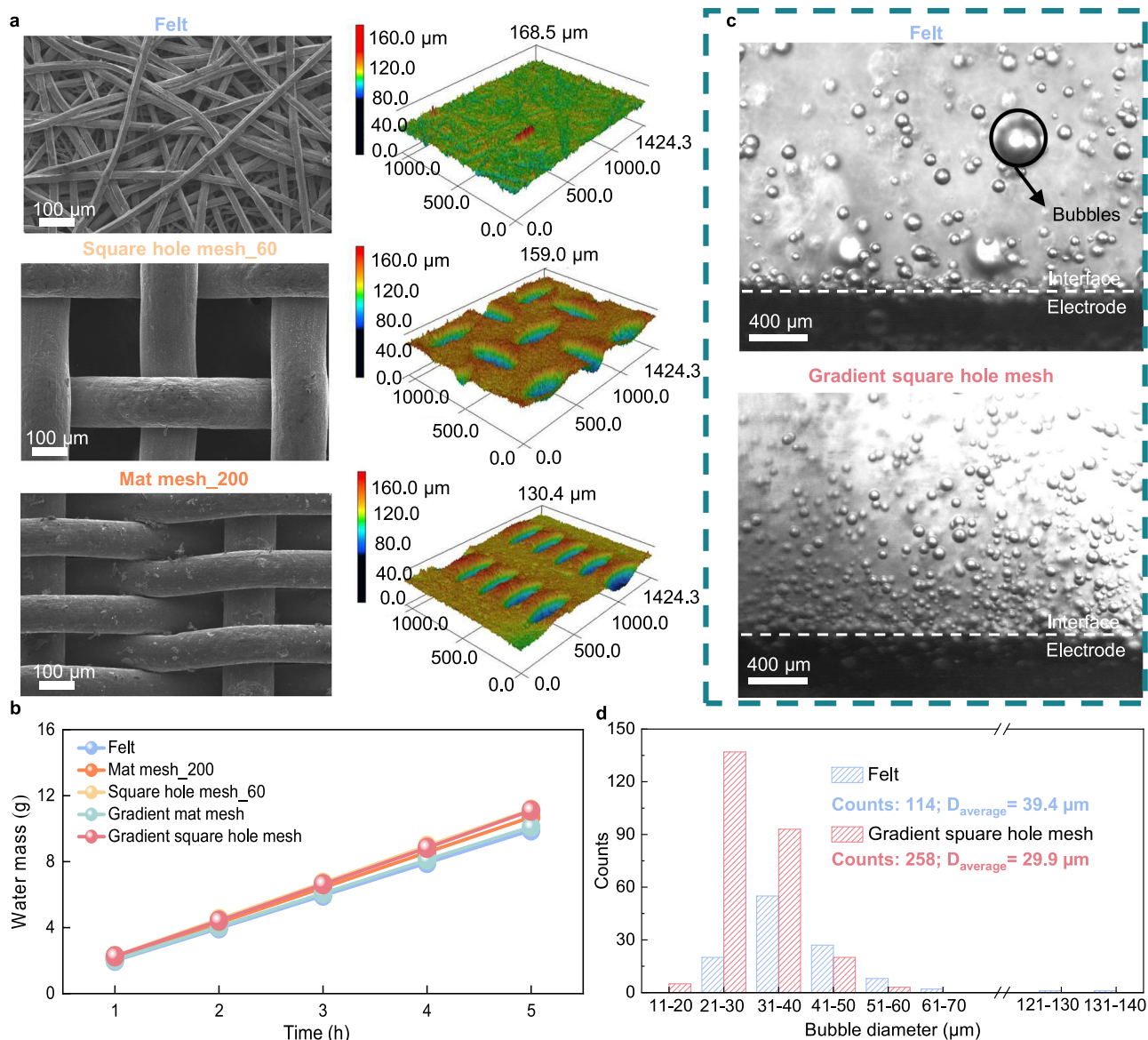


Fig. 6 | Electrode designs influence bubble and water management. **a** SEM, confocal laser scanning microscope photograph, and surface height information of felt, mat mesh with sieves of 1250 and square hole mesh with sieves of 60. Scale bar: 100 μm . **b** The amount of water collected at the cathode across the membrane as a function of time for AMEWES with different stainless steel electrode designs.

c Bubble behaviors in different stainless steel electrode designs. (operating conditions: room temperature ($25 \pm 2^\circ\text{C}$), 0.4 A cm^{-2} , three electrode H-cell tests, in-plane direction parallel to the ground). Scale bar: 400 μm . **d** The distribution of bubble sizes counted in high-speed camera images. Source data are provided as a Source Data file.

inferiority to the gradient square hole mesh can be explained by the higher cathode activation and mass transport impedance than that of the gradient square hole mesh. It can be seen that the layer of the gradient mat mesh close to the membrane has 1250 sieves. The sieve pore is too small for the diffusion of liquid water from the anode to the cathode, as shown in Fig. 6b. In the potential measurements, the gradient square hole mesh ensures that the anode potential is comparable to that of the felt but ensures that the overpotential of the cathode is much higher than that of the felt (Fig. 5e), which also doubly confirms that this design improves the overall electrochemical performance of AEMWE.

In the microscale visualization and quantitative statistics of the bubble behaviors (Fig. 6c, d) (also see Supplementary Movie 3), the number of bubbles removal from the gradient square hole mesh more than tripled (114 to 258 counts) and the diameter decreases from 39.4 to 29.9 μm compared to that of the felt, which is also responsible for the highest amount of cathode liquid water collected (Fig. 6b). In

addition, the bubble behaviors of mat mesh, square hole mesh, and gradient mat mesh are also provided in Supplementary Fig. 34. The bubble behaviors of the electrodes also affect the millimeter-scale two-phase flow regimes in the flow field (also see Supplementary Movie 4). As shown in Fig. 7a, b, decreased bubbles clogging in the flow field caused by the gradient square hole mesh will cover less electrode area compared to the stainless steel felt. Specifically, Fig. 7c demonstrates that the difference in the proportion of plug, slug, and large bubble flow in the flow field caused by the two electrodes is small at low current densities. However, the ratio of effective area and dense tiny bubbles flow in the flow field caused by the gradient square hole mesh is significantly higher compared to the stainless steel felt, and this is especially evident at higher current densities, e.g., 3.0 A cm^{-2} . Therefore, it can be hypothesized that the dense tiny bubbles flow does not cover the electrodes and affects the mass transport of water. Finally, we further investigate the durability of the gradient square hole mesh. The AEMWE fitted with this design was operated under anode-feeding

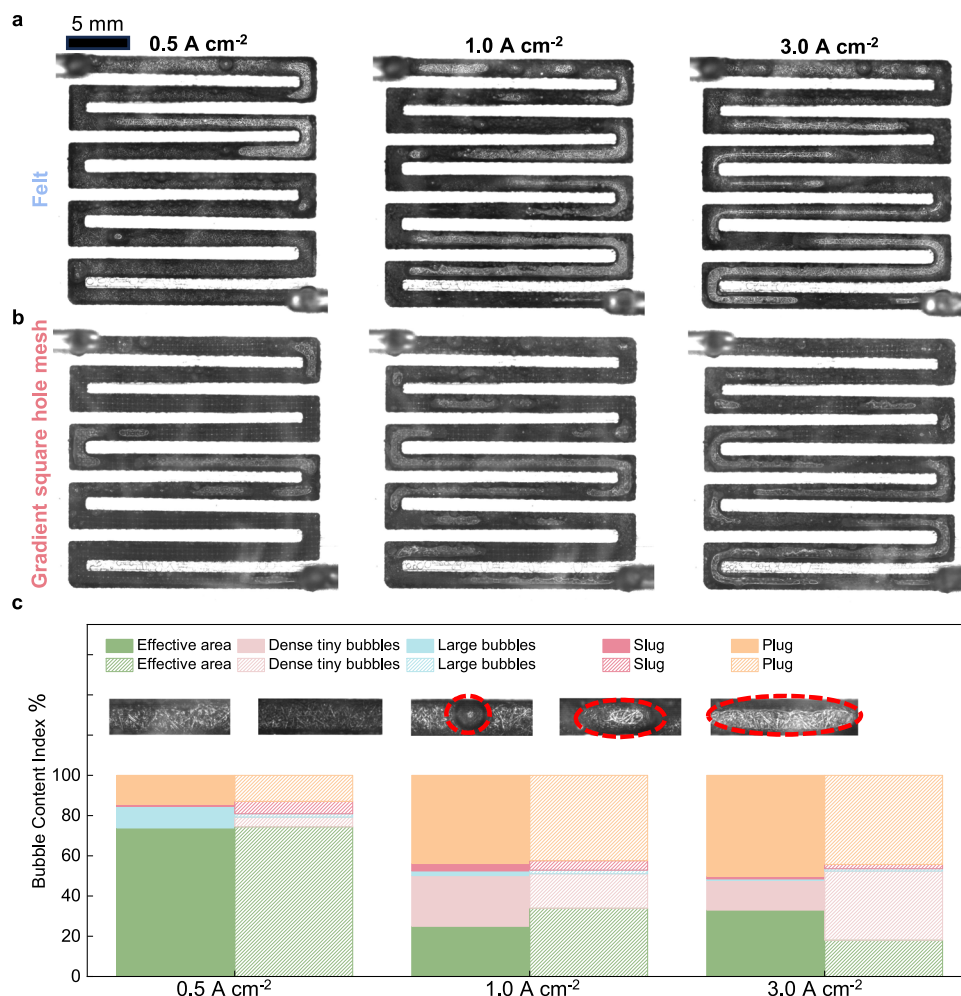


Fig. 7 | Two-phase flow visualization and regime distribution in flow fields. **a** Stainless steel felt, **b** gradient stainless steel square hole mesh. **c** Distribution of different flow regimes in the flow field. The inset image above the bar chart defines the categories in the legend: Effective area (no bubble accumulation); Dense tiny

bubbles (high concentration of discrete micro-bubbles); Large bubbles (individual coalesced bubbles); Slug (channel width < bubble length < 3 times channel width); and Plug (bubble length > 3 times channel width). Source data are provided as a Source Data file.

(dry cathode) conditions and fed with 0.1 M KOH to the anode. Stable operation for 400 h (degradation rate: 0.035 mV h⁻¹) at a current density of 1 A cm⁻² (Fig. 5f) demonstrated its competitive application prospects compared with reported electrodes (Supplementary Table 2) in AEMWE.

For our laboratory-scale cell operating at high current densities (e.g., 5.0 A cm⁻²), low flow rates such as 1.0 and 3.0 mL min⁻¹ fail to ensure adequate delivery of KOH solution to the anode electrode. Blindly increasing the KOH flow rate to 30 mL min⁻¹ does not effectively enhance AEMWE performance as the gradient square hole mesh does and may even prove counterproductive (Supplementary Fig. 35a, b). Therefore, 5.0 mL min⁻¹ represents the optimal flow rate at high current densities (Supplementary Fig. 35b). While higher flow rates promote bubble removal in flow channels (Supplementary Fig. 36), increased velocity toward the electrode in the Y-direction impedes bubble removal within the electrode (Supplementary Fig. 37), raising impedances for OER, mass transport, HER, and OH⁻ transport (Supplementary Fig. 35c). Additionally, higher flow rates waste electrical energy and are not recommended. Therefore, optimizing electrode structures to overcome bubble clogging at high current densities may be a better solution. Finally, it is also worth emphasizing that the cost of a traditional IrO₂ electrode is the highest, estimated at over \$111,000/m². In comparison, 316 L stainless steel mesh costs about \$8–150/m², which is even lower than the over \$7,200/m² for 316 L

stainless steel felt, over \$4,200/m² for Ni felt, and over \$350/m² for Ni mesh. More details about the cost analysis of anode electrodes can be found in Supplementary Table 3. The gradient stainless steel mesh not only enhances electrolysis efficiency but also simplifies the preparation process, leading to a significant 99.86% reduction in anode manufacturing costs compared with the traditional IrO₂ electrode. Thus, it presents a cost-effective and efficient alternative to traditional electrodes.

Discussion

In summary, this study demonstrates that bubble dynamics plays a major role in limiting the performance of AEMWE at industrially relevant current densities, highlighting that its optimization is as important as maximizing ECSA. By systematically analyzing pore size and surface wettability of stainless steel electrodes, we demonstrate that bubble accumulation at the anode covers active sites at the anode, hinders water diffusion through the membrane, and further causes water shortage at the cathode, collectively degrading electrolysis efficiency. Conventional stainless steel felt, despite higher ECSA, suffering from severe bubble coverage (average bubble diameter: 39.4 μm). Based on the above mechanism, the proposed gradient stainless steel square hole mesh mitigates this issue by ensuring minimal ECSA requirements, enabling simultaneous fast bubble removal and water diffusion. It features a sparse outer layer (60 sieves)

and a dense inner layer (200 sieves). Compared with the felt, the average bubble diameter decreased by 24% to 29.9 μm , while the bubble detachment number increased twofold (258 vs. 114 counts). And this gradient design shifts two-phase flow regimes in the flow field from plug flow to dense tiny bubbles and effective areas. In addition, the gradient stainless steel square hole mesh is simple and easy to prepare. It has demonstrated very good stability (400 h of operation with a decay rate of 0.035 mV h^{-1} only), and its cost is only around \$8–150/ m^2 , much lower than traditional titanium fiber felt coated with IrO_2 (> \$111,000/ m^2). Most importantly, our findings underscore the significance of two-phase flow management. Strategies such as gradient open pore designs to regulate bubble and water transport present a promising direction for electrode engineering. Future work should integrate machine learning with additive manufacturing to optimize similar hierarchical structures, potentially bridging the gap between laboratory research and large-scale implementation at industrially relevant current densities (>1.0 A cm^{-2}).

Methods

Materials

The experimental materials include 316 L stainless steel felt and 316 L stainless steel mesh from Fuershun Electronic Materials and carbon paper (TGP-H-090) from Toray Co., Japan; Pt/C (60%) catalyst from Johnson Matthey (UK); PiperION A membrane (60 μm) and Nafion ionomer (D520, 5 wt %) from Fuel Cell Store (USA); Potassium hydroxide (KOH) (Macklin, 95%) from Shandong Keyuan Biochemical Co., Ltd; Iridium oxide powder (IrO_2 , 99%) from Alfa Aesar. All chemicals are stored in dedicated chemical cabinets and are used without any further processing.

Preparation of membrane electrode assemblies

Stainless steel felts and meshes were cut into 4 cm^2 (2.0 \times 2.0 cm) and were cleaned in an ultrasonic bath with ethanol and DI water for 30 min, respectively. The catalyst loading was determined by the mass of catalyst in the ink divided by the coated geometric area (4 cm^2). The catalyst loading of the cathode is 0.5 mg cm^{-2} and the catalyst ink was prepared by mixing 60 wt% Pt/C with ionomer (D520, 5 wt%) at a mass ratio of 4:1, and then ethanol was added into the solution as a solvent⁴¹. Subsequently, the ink was subjected to dispersion within an ultrasonic ice bath for 30 min⁴². Thereafter, the ink was sprayed onto the carbon paper and dried repeatedly, until the catalyst loading reached the desired value⁴³. For the membrane, the square PiperION A (60 μm) were cut into 6.25 cm^2 (2.5 \times 2.5 cm) small pieces and were immersed in 1.0 M KOH solution at room temperature (25 \pm 2 $^\circ\text{C}$) for 24 h before being incorporated into the MEA³². Finally, MEA was created by combining an anode stainless steel electrode and cathode Pt-based carbon paper electrode with a PiperION A membrane in the middle.

For the anode porous transport electrodes used in AEMWE, the anode ink composed of IrO_2 and ionomer was directly deposited onto 4 cm^2 (2.0 \times 2.0 cm) stainless steel felts via spray coating. The anode catalyst ink was prepared by bath sonication of a mixture containing the ionomer (either Nafion D520 or PiperION A), commercially available IrO_2 catalyst with an Ionomer: Catalyst ratio of 0.4, isopropyl alcohol, and deionized water for 40 min. The resulting ink was then sprayed onto the electrode to achieve a catalyst loading of 1.6 mg cm^{-2} .

Acid treatment

Firstly, stainless steel felts were cut into 4 cm^2 (2.0 \times 2.0 cm) and were cleaned in an ultrasonic bath with ethanol for 30 mins, respectively. After drying at 60 $^\circ\text{C}$, stainless steel felt is then immersed in the pickling solution to form a rough topography to obtain a hydrophilic surface, but cause fiber surface oxidation. The pickling solution was prepared by combining 200 mL of deionized (DI) water with 25 mL of 70% nitric acid and then heating it to a temperature of 60 $^\circ\text{C}$ (\pm 5 $^\circ\text{C}$). A stainless steel felt sample measuring 4 cm^2 (2.0 \times 2.0 cm) was weighed

prior to the procedure. The sample was immersed in the solution for 10 min with vigorous stirring. Following this, the sample was thoroughly rinsed with DI water and dried in an oven at 100 $^\circ\text{C}$.

Hydrochloric acid (HCl) treatment can etch stainless steel fibers without causing fiber surface oxidation. The pickling solution was prepared by combining 150 mL of deionized (DI) water with 50 mL of 37% nitric acid and then heating it to a temperature of 60 $^\circ\text{C}$ (\pm 5 $^\circ\text{C}$). Two stainless steel mat mesh samples measuring 4 cm^2 (2.0 \times 2.0 cm). The samples were immersed in the solution for 30 and 60 min, respectively, with vigorous stirring. Following this, the samples were also thoroughly rinsed with DI water and dried in an oven at 100 $^\circ\text{C}$.

Characterization of anode stainless steel electrodes

The morphology and elemental composition of anode stainless steel felts and stainless steel meshes were characterized using SEM (TESCAN MIRA LMS, Czech) with energy-dispersive X-ray spectroscopy mapping. The elements on the fiber surface were also determined by X-ray photoelectron spectroscopy (XPS) (Thermo Scientific K-Alpha Nexsa). The liquid water contact angle test (Biolin Scientific Theta Lite) is employed to assess the rate at which liquid water penetrates the alcohol-washed and acid-washed stainless steel felts. A confocal laser scanning microscope (KEYENCE VK-X200) was used to characterize the structure of stainless steel felts and stainless steel meshes. The pore size distributions of the anode stainless steel felts with different pore sizes were measured by Mercury Intrusion Porosimetry (Micromeritics AutoPore IV 9510).

AEMWE fabrication and assembly

The AEMWE was constructed using a home-made fixture with serpentine flow fields. They are made of nickel (anode) and titanium (cathode), with a depth of 1.0 mm each. In order to prevent electrolyte leakage, fluorine rubber gaskets with a thickness of 0.4 mm were placed between the two half fixtures. In the middle of the two flow field plates is the prepared MEA. Before testing, the cathode and anode electrodes are soaked in fresh 1 M KOH for 1 h³². Before starting the experiment each day, the specific steps for preparing the electrolyte (1 M KOH) are as follows: dissolve the potassium hydroxide particles in deionized water in a fume hood. After preparing 1000 mL of 1 M KOH electrolyte each time, store it in a sealed glass bottle, and prepare the solution used every day to ensure it is not contaminated. The cell was clamped by anode and cathode stainless steel end plates with four equally distributed bolts (3.0 N·m torque in each bolt).

Electrochemical measurements

During the experimental procedure, the AEMWE was heated and maintained at 80 $^\circ\text{C}$. A peristaltic pump (BT100-2J from LongerPump) was employed to continuously deliver a 1 M KOH solution to the anode inlet of the AEMWE at a mass flow rate of 5 ml min^{-1} . To ensure stable and reliable performance, the cell underwent a conditioning process (approximately 100 cycles of CV from 1.4 to 2.5 V)⁴⁴.

For the electrochemical characterization of the AEMWE, an Autolab PGSTAT302N electrochemical workstation, equipped with an additional booster, was utilized. Initially, polarization curves were measured over a current density range of 0 A cm^{-2} to 5.0 A cm^{-2} . The AEMWE was operated for 100 s at each specific point under low current densities (<1.0 A cm^{-2}) and 300 s at each specific point high current densities (>1.0 A cm^{-2}) to reach a steady state, and the cell voltage was recorded by averaging the voltage values over the last 10 s at each operating point. Subsequently, electrochemical impedance spectroscopy (EIS) measurements were conducted across a frequency range of 40 kHz to 1 Hz.

In the durability testing phase, a 0.1 M KOH solution replaced the previously used 1 M KOH solution for the anode feed. The electrolyte was replenished with water every 24 h to maintain a consistent KOH concentration throughout the experiment. A KUAQU DC power

supply was used to supply current, and the cell voltage was recorded every two hours by means of a paperless recorder.

Breakdown of overpotentials

Tafel approximation^{45–47}, can be used to calculate the mass transport overpotential of AEMWE. The method involves the following steps. First, the total cell voltage (E_{cell}) was measured, and the HFR (R_{ohmic}) was obtained from EIS tests. Next, the ohmic overpotential (η_{ohmic}) was calculated by Eq. (1). For the kinetic analysis, the activation overpotential ($\eta_{\text{activation}}$) was described by the Tafel equation (Eq. (2)). The parameters b and i_0 were obtained by fitting the iR -free curves ($E_{\text{cell}} - \eta_{\text{ohmic}}$). Finally, the mass transport overpotential ($\eta_{\text{mass transport}}$) was obtained by Eqs. (3) and (4). The relative equations are as follows:

$$\eta_{\text{ohmic}} = iR_{\text{ohmic}} \quad (1)$$

$$\eta_{\text{activation}} = b \log_{10} \left(\frac{i}{i_0} \right) \quad (2)$$

$$E_{\text{rev}} = 1.5184 - 1.5421 \times 10^{-3} T + 9.523 \times 10^{-5} T \ln T + 9.84 \times 10^{-8} T^2 \quad (3)$$

$$\eta_{\text{mass transport}} = E_{\text{cell}} - E_{\text{rev}} - \eta_{\text{activation}} - \eta_{\text{ohmic}} \quad (4)$$

where T (K) is the temperature. i (A cm^{-2}) is the current density.

Distribution of relaxation times (DRT) analysis

The DRT method directly derives electrochemical system relaxation characteristics from impedance spectra. It transforms frequency-domain impedance data into time-domain relaxation time distributions, enabling differentiation of primary and secondary electrochemical reaction processes⁴⁸. Since electrochemical system polarization impedance is constant and the frequency in the EIS is usually set according to the logarithmic interval, the impedance reconstructed using DRT is typically described by Eq. (5).

$$Z_{\text{DRT}}(f) = R_0 + \int_{-\infty}^{+\infty} \frac{\gamma(\ln\tau)}{1 + j2\pi f\tau} d\ln\tau \quad (5)$$

Where $Z_{\text{DRT}}(f)$ represents the total impedance of the electrochemical system (in the complex plane), R_0 represents the ohmic impedance, that is, the impedance value of the electrochemical system when the frequency is infinite, j is an imaginary unit, τ is the characteristic relaxation time, and f is the frequency. Building on the DRTtools framework developed by Ciucci et al.^{49,50}, a genetic algorithm optimizes the frequency factor for a DRT-based EIS reconstruction method.

DRT peaks correspond to electrochemical reaction processes. The identification of the peaks was guided by characteristic frequencies summarized in literature for different electrochemical systems⁵¹, along with our previous research³⁵. Specifically, the first peak appears in the range of 1–10 Hz, and is attributed to mass transport processes related to water/gas transfer. The second peak, observed in the range of 50–200 Hz, corresponds to the OER. The third peak, located at 300–800 Hz, is associated with the HER. Notably, the time constants for OER and HER differ by approximately one order of magnitude, allowing them to be clearly distinguished in the DRT plot. The fourth peak, found at frequencies above 1000 Hz, is typically linked to ionic transport processes occurring within the CL or at the interfaces.

Electrochemically active surface area (ECSA) calculation

The ECSA of the stainless steel electrodes was evaluated and compared based on their double-layer capacitance (C_{dl}). The measurements were

conducted in a standard three-electrode configuration within a non-Faradaic potential window (0.774–0.974 V vs. RHE in 1.0 M KOH). CVs were recorded at scan rates from 40 to 160 mV s^{-1} . The capacitive current ($\Delta j = (j_{\text{a}} - j_{\text{c}})/2$) at the central potential of 0.874 V vs. RHE was plotted against the scan rate. The slope of this linear plot corresponded to C_{dl} . Since all electrodes are made from the same 316 L stainless steel material, their specific capacitance (C_{s}) remains unchanged. Therefore, C_{dl} is directly proportional to the ECSA, and a direct comparison of C_{dl} values is valid for assessing their relative active surface areas.

High-speed visualization system

For observing micrometer-scale bubble behavior on the electrode surfaces (Supplementary Fig. 1), the Revealer M230M camera, coupled with a microscope, enabled clear visualizations. To record these bubble behaviors, an exposure of 5000 was used, again with a frame rate of 1000 fps. Two videos were captured, illustrating bubble behavior at the surfaces of stainless steel felt and stainless steel gradient square hole mesh, at a current density of 0.4 A cm^{-2} . The experimental setup consisted of a three-electrode electrochemical measurement conducted in a square H-cell (Working electrode: stainless steel electrode, counter electrode: Pt sheet, reference electrode: Hg/HgO (1.0 M KOH), electrolyte: 1.0 M KOH, 200 mL per compartment). For quantitative analysis of bubble distribution, the bubble visualization image is first binarized and a hole-filling algorithm (BW) is applied. Then, the regionprops function is used to identify and extract parameters such as bubble size and count⁵².

The Revealer M230M high-speed camera, paired with microscale lenses, was utilized to visualize millimeter-scale two-phase flow within the flow field (Supplementary Fig. 1). In this investigation, a recording frame rate of 500 fps and an exposure of 500 were selected to capture the dynamics of the two-phase flow. Six videos were recorded, showcasing the two-phase flow in a configuration comprising stainless steel felt and stainless steel gradient square hole mesh, at current densities of 0.5, 1.0, and 3.0 A cm^{-2} .

Three electrode measurements

Three electrode testing was conducted using 1.5 × 1.5 cm stainless steel felts or meshes as the working electrode, an Hg/HgO electrode as the reference, and a Pt sheet (1.5 × 1.5 cm) as the counter electrode in 1.0 M KOH (100 mL) at room temperature (25 ± 2 °C). For Hg/HgO reference electrode, it was calibrated against a reversible hydrogen electrode (RHE) in H_2 -saturated 1.0 M KOH at room temperature (25 ± 2 °C) using a Pt sheet as both working and counter electrode. The average potential was +0.926 V vs. RHE and was used for all potential conversions in three-electrode tests. The anode electrodes underwent conditioning by conducting 10 cyclic voltammetry sweeps within the voltage range of 0.3–2.0 V versus Hg/HgO. Subsequently, their performance was evaluated using linear sweep voltammetry from 0.3 to 2.0 V versus Hg/HgO at a scan rate of 10 mV s^{-1} . To assess the electrolyte resistance and apply iR correction, potentiostatic EIS was performed at the open circuit voltage.

Anode potential and cathode potential test

The anode potential of this AEMWE was recorded in conjunction with the polarization curve test at room temperature (25 ± 2 °C). The cathode potential is calculated by the equation below:

$$V_{\text{c}} = V_{\text{a}} - E_{\text{cell}} \quad (6)$$

V_{c} (V) and V_{a} (V) denote the anode and cathode potentials, respectively. The anode serves as the working electrode, while the cathode acts as the counter electrode. A 3 mm thick Hg/HgO electrode is utilized as the reference electrode. The potential of the anode is determined by using the open-circuit potential technique with the

CHI650E electrochemical workstation. The anode flow field plate features a 4 mm diameter hole that connects to the anode channel inlet, allowing for the insertion of the Hg/HgO reference electrode, which is sealed using PEEK plastic, as shown in Supplementary Fig. 2. By minimizing the distance between the anode and the Hg/HgO reference electrode, the measurement of the anode potential is enhanced in terms of accuracy⁵³.

Water diffusion measurements

We use anode-feeding mode, the cathode inlet is closed. At the anode there is diffusion of water to the cathode and some of the water undergoes HER at the cathode. The unreacted water is pushed to the cathode outlet by the hydrogen gas produced and is collected by silica gel particles, as shown in Supplementary Fig. 3. The weight of the collected water is recorded every hour.

Data availability

The data generated in this study are provided in the Supplementary Information/Source Data file. Source data are provided with this paper.

References

1. Lee, J. K. et al. Ionomer-free and recyclable porous-transport electrode for high-performing proton-exchange-membrane water electrolysis. *Nat. Commun.* **14**, 4592 (2023).
2. Lee, B., Wang, L., Wang, Z., Cooper, N. J. & Elimelech, M. Directing the research agenda on water and energy technologies with process and economic analysis. *Energy Environ. Sci.* **16**, 714–722 (2023).
3. Terlouw, T., Bauer, C., McKenna, R. & Mazzotti, M. Large-scale hydrogen production via water electrolysis: a techno-economic and environmental assessment. *Energy Environ. Sci.* **15**, 3583–3602 (2022).
4. Ikuero, T., Bade, S. O., Akinmoladun, A. & Oni, B. A. The integration of wind and solar power to water electrolyzer for green hydrogen production. *Int. J. Hydrogen Energy* **76**, 75–96 (2024).
5. Du, N. et al. Anion-exchange membrane water electrolyzers. *Chem. Rev.* **122**, 11830–11895 (2022).
6. Yang, Y. et al. Anion-exchange membrane water electrolyzers and fuel cells. *Chem. Soc. Rev.* **51**, 9620–9693 (2022).
7. Li, Z. et al. Seed-assisted formation of NiFe anode catalysts for anion exchange membrane water electrolysis at industrial-scale current density. *Nat. Catal.* **7**, 944–952 (2024).
8. Liu, J. et al. Synergistic promotion by highly active square-shaped lead oxide and visualized electrolyzer for enhanced electrochemical ozone production. *Chin. J. Catal.* **57**, 80–95 (2024).
9. Tang, J., Guo, K., Guan, D., Hao, Y. & Shao, Z. A semi-vapor electrolysis technology for hydrogen generation from wide water resources. *Energy Environ. Sci.* **17**, 7394–7402 (2024).
10. Pham, C. V., Escalera-López, D., Mayrhofer, K., Cherevko, S. & Thiele, S. Essentials of high performance water electrolyzers – from catalyst layer materials to electrode engineering. *Adv. Energy Mater.* **11**, 2101998 (2021).
11. Zhang, L., Shi, Z., Lin, Y., Chong, F. & Qi, Y. Design strategies for large current density hydrogen evolution reaction. *Front. Chem.* **10**, 866415 (2022).
12. Wan, L. et al. Key components and design strategy of the membrane electrode assembly for alkaline water electrolysis. *Energy Environ. Sci.* **16**, 1384–1430 (2023).
13. Jin, H. et al. Nanocatalyst design for long-term operation of proton/anion exchange membrane water electrolysis. *Adv. Energy Mater.* **11**, 2003188 (2021).
14. Jiang, W. et al. Composition-dependent morphology, structure, and catalytic performance of nickel-iron layered double hydroxide as highly-efficient and stable anode catalyst in anion exchange membrane water electrolysis. *Adv. Funct. Mater.* **32**, 2203520 (2022).
15. Xu, Q. et al. Anion exchange membrane water electrolyzer: electrode design, lab-scaled testing system and performance evaluation. *EnergyChem* **4**, 100087 (2022).
16. Park, J. E. et al. Three-dimensional unified electrode design using a NiFeOOH catalyst for superior performance and durable anion-exchange membrane water electrolyzers. *ACS Catal.* **12**, 135–145 (2022).
17. Klingenhof, M. et al. Anion-tuned layered double hydroxide anodes for anion exchange membrane water electrolyzers: from catalyst screening to single-cell performance. *ACS Energy Lett.* **7**, 3415–3422 (2022).
18. Lu, X. et al. Unveiling micro- and nanoscale bubble dynamics for enhanced electrochemical water splitting. *Adv. Colloid Interface Sci.* **343**, 103544 (2025).
19. Kempler, P. A., Coridan, R. H. & Luo, L. Gas evolution in water electrolysis. *Chem. Rev.* **124**, 10964–11007 (2024).
20. Lu, X. et al. Evolution of hydrogen bubbles on a microelectrode driven by constant currents and its impact on potential response. *Chem. Eng. J.* **500**, 156890 (2024).
21. Hu, C. et al. Advanced patterned membranes for efficient alkaline membrane electrolyzers. *ACS Energy Lett.* **9**, 1219–1227 (2024).
22. Xu, W., Lu, Z., Sun, X., Jiang, L. & Duan, X. Superwetting electrodes for gas-involving electrocatalysis. *Acc. Chem. Res.* **51**, 1590–1598 (2018).
23. Qiu, J. et al. Enhancing water electrolysis performance by bubble behavior management. *Small Methods.* **9**, 2402105 (2025).
24. Li, M., Xie, P., Yu, L., Luo, L. & Sun, X. Bubble engineering on micro/nanostructured electrodes for water splitting. *ACS Nano* **17**, 23299–23316 (2023).
25. Dong, Y. et al. Superhydrophilic/superaerophobic NiFe with internal bubble flow channels for electrocatalytic water splitting. *Chem. Eng. J.* **488**, 150953 (2024).
26. Shen, J., Zheng, Y., Lei, W. & Shao, H. Unraveling the fundamental concepts of superaerophobic/superhydrophilic electrocatalysts for highly efficient water electrolysis: implications for future research. *ChemElectroChem* **11**, e202300465 (2024).
27. Andaveh, R., Barati Darband, G. H., Maleki, M. & Sabour Rouhaghdam, A. Superaerophobic/superhydrophilic surfaces as advanced electrocatalysts for the hydrogen evolution reaction: a comprehensive review. *J. Mater. Chem. A* **10**, 5147–5173 (2022).
28. Wan, L. et al. 3D-ordered catalytic nanoarrays interlocked on anion exchange membranes for water electrolysis. *Energy Environ. Sci.* **17**, 3396–3408 (2024).
29. Ding, S. et al. Enhancing mass transfer in anion exchange membrane water electrolysis by overlaid nickel mesh substrate. *ACS Energy Lett.* **9**, 3719–3726 (2024).
30. Wu, L. et al. A dual-layer flow field design capable of enhancing bubble self-pumping and its application in water electrolyzer. *Chem. Eng. J.* **488**, 151000 (2024).
31. Wu, L. et al. Optimization of dual-layer flow field in a water electrolyzer using a data-driven surrogate model. *Energy AI* **18**, 100411 (2024).
32. Tricker, A. W. et al. Pathways toward efficient and durable anion exchange membrane water electrolyzers enabled by electro-active porous transport layers. *Adv. Energy Mater.* **14**, 2303629 (2024).
33. Xu, Q. et al. Integrated reference electrodes in anion-exchange-membrane electrolyzers: impact of stainless-steel gas-diffusion layers and internal mechanical pressure. *ACS Energy Lett.* **6**, 305–312 (2021).
34. Zuo, Y. et al. Stainless steel activation for efficient alkaline oxygen evolution in advanced electrolyzers. *Adv. Mater.* **36**, 2312071 (2024).

35. Wu, L. et al. Unrevealing the interaction between electrode degradation and bubble behaviors in an anion exchange membrane water electrolyzer. *Adv. Sci.* **12**, 2412962 (2025).
36. Tricker, A. W. et al. Design and operating principles for high-performing anion exchange membrane water electrolyzers. *J. Power Sources* **567**, 232967 (2023).
37. Wan, L. et al. Construction of integrated electrodes with transport highways for pure-water-fed anion exchange membrane water electrolysis. *Small* **18**, 2200380 (2022).
38. Yuan, S. et al. Bubble evolution and transport in PEM water electrolysis: mechanism, impact, and management. *Prog. Energy Combust. Sci.* **96**, 101075 (2023).
39. Lu, X. et al. How dual hydrogen bubble evolution inhibits electrolytic performance. *J. Power Sources* **632**, 236356 (2025).
40. Lu, X. et al. Hydrogen bubble evolution and gas transport mechanism on a microelectrode determined by cathodic potential and temperature. *Phys. Fluids* **36**, 073302 (2024).
41. Li, W. et al. Performance of a hybrid direct ammonia fuel cell with hydrogen peroxide reduction. *J. Power Sources* **593**, 233985 (2024).
42. Pan, Z. et al. Overall design of a gradient-ordered membrane electrode assembly for direct liquid fuel cells. *Adv. Funct. Mater.* **34**, 2404710 (2024).
43. Pan, Z. et al. Engineered wettability-gradient porous structure enabling efficient water manipulation in regenerative fuel cells. *Energy AI* **17**, 100400 (2024).
44. Wang, W. et al. Exploring the impacts of conditioning on proton exchange membrane electrolyzers by in situ visualization and electrochemistry characterization. *ACS Appl. Mater. Interfaces* **14**, 9002–9012 (2022).
45. Zhao, B. et al. Superhydrophilic porous transport layer enhances efficiency of polymer electrolyte membrane electrolyzers. *Cell Rep. Phys. Sci.* **2**, 100580 (2021).
46. Kim, P. J. et al. Tailoring catalyst layer interface with titanium mesh porous transport layers. *Electrochim. Acta* **373**, 137879 (2021).
47. Yuan, S. et al. Bubble management in PEM water electrolysis via imprinting patterned grooves on catalyst layer. *Int. J. Heat Mass Transfer* **212**, 124249 (2023).
48. Wang, Q. et al. A comparative study of equivalent circuit model and distribution of relaxation times for fuel cell impedance diagnosis. *Int. J. Energy Res.* **45**, 15948–15961 (2021).
49. Quattrocchi, E. et al. Deconvolution of electrochemical impedance spectroscopy data using the deep-neural-network-enhanced distribution of relaxation times. *Electrochim. Acta* **439**, 141499 (2023).
50. Maradesa, A. et al. Advancing electrochemical impedance analysis through innovations in the distribution of relaxation times method. *Joule* **8**, 1958–1981 (2024).
51. Ranz, M., Grabner, B., Schweighofer, B., Wegleiter, H. & Trattner, A. Dynamics of anion exchange membrane electrolysis: unravelling loss mechanisms with electrochemical impedance spectroscopy, reference electrodes and distribution of relaxation times. *J. Power Sources* **605**, 234455 (2024).
52. Dezső-Weidinger, G., Stitou, A., Van Beeck, J. & Riethmüller, M. L. Measurement of the turbulent mass flux with PTV in a street canyon. *J. Wind. Eng. Ind. Aerodyn.* **91**, 1117–1131 (2003).
53. Li, W. et al. Monitoring ammonia and water transport through anion exchange membranes in direct ammonia fuel cells. *J. Power Sources* **628**, 235900 (2025).

Acknowledgements

This work was supported by a grant from the Research Grants Council of the Hong Kong Special Administrative Region, China (Project No. 15308024) (received by L.A.) and by a grant from Research Centre for Carbon-Strategic Catalysis (RC-CSC), The Hong Kong Polytechnic University (CE2X) (received by L.A.).

Author contributions

L.W. conceptualized the study, developed the methodology, performed the experiments, and prepared the original draft. Q.W., S.Y., and W.L. performed the investigation and validation. X.Z., M.T., and K.Z. helped polish the language. X.Y. and L.A. supervised the project and participated in the review. All authors commented on the manuscript.

Competing interests

The authors declare no competing interests.

Additional information

Supplementary information The online version contains supplementary material available at <https://doi.org/10.1038/s41467-026-69052-5>.

Correspondence and requests for materials should be addressed to Xiaohui Yan or Liang An.

Peer review information *Nature Communications* thanks Dengwei Jing and the other anonymous reviewer(s) for their contribution to the peer review of this work. A peer review file is available.

Reprints and permissions information is available at <http://www.nature.com/reprints>

Publisher's note Springer Nature remains neutral with regard to jurisdictional claims in published maps and institutional affiliations.

Open Access This article is licensed under a Creative Commons Attribution-NonCommercial-NoDerivatives 4.0 International License, which permits any non-commercial use, sharing, distribution and reproduction in any medium or format, as long as you give appropriate credit to the original author(s) and the source, provide a link to the Creative Commons licence, and indicate if you modified the licensed material. You do not have permission under this licence to share adapted material derived from this article or parts of it. The images or other third party material in this article are included in the article's Creative Commons licence, unless indicated otherwise in a credit line to the material. If material is not included in the article's Creative Commons licence and your intended use is not permitted by statutory regulation or exceeds the permitted use, you will need to obtain permission directly from the copyright holder. To view a copy of this licence, visit <http://creativecommons.org/licenses/by-nc-nd/4.0/>.

© The Author(s) 2026